Correction of distorted X-ray absorption spectra collected with capillary sample cell

Hao Wang [a, b], Yuecheng Lai [a, b], Jiajun Zhong [a, b], Yunpeng Liu [a], Lei Yao [a], Lixiong Qian [c], Xueqing Xing [a], Zhongjun Chen [a], Guang Mo [a, *], Zhonghua Wu [a, b, *]

[a] Beijing Synchrotron Radiation Facility, Institute of High Energy Physics, Chinese Academy of Sciences, Beijing 100049, China

[b] University of Chinese Academy of Sciences, Chinese Academy of Sciences, Beijing 100049, China

[c] School of Materials Science and Engineering, Northeastern University, Shenyang 110819, PR China

*: Correspondence to: Zhonghua Wu, E-mail: wuzh@ihep.ac.cn

Guang Mo, E-mail: mog@ihep.ac.cn

Abstract:

In certain exceptional cases, capillary samples must be used to measure X-ray absorption spectra (XAS). However, the inhomogeneous thickness of capillary samples causes XAS distortion. This study discusses the distortion and correction of the XAS curve caused by the inhomogeneous thickness of capillary samples. The relationship between the distorted XAS curve $\mu' d_{eq}$ (measured values) and the real absorption coefficient $\mu_s d_{eq}$ (true values) of the sample was established. The distortion was slight and negligible when the vertical size ($2h$) of the X-ray beam spot was smaller than 60% of the capillary tube's inner diameter ($2R_{in}$). When $h/R_{in} > 1$, X-ray leakage is inevitable and should be avoided during measurement. Partial X-ray leakage caused by an X-ray beam spot size larger than the inner diameter of the capillary tube leads to serious compressed distortion of the XAS curve. When $h/R_{in} < 1$, the distorted XAS data were well corrected. Possible errors and their influence on the corrected XAS are also discussed. Simulations and corrections for distortions verify the feasibility and effectiveness of the corrected method.

Key words: XAS, Capillary, Compression distortion, Correction, Python

1. Introduction

The X-ray Absorption Fine Structure (XAFS) technique is widely used to characterize the chemical valence and coordination environments of elements in materials [1, 2]. XAFS has been widely used in research on in situ dynamic processes due to its sensitivity to local atomic structures. For example, research on element chemical valence changes during the charging and discharging of batteries [3-7], determination of active sites in catalytic reactions [8-11], and nucleation and growth in the synthesis of nanomaterials [12]. In situ sample environment systems and sample cells are indispensable in realizing in situ (or operando) XAFS measurements. In providing in situ experimental conditions, the sample cells often need to be specially designed, even those with an irregular shape [13-15]. For instance, the in situ Small Angle X-ray Scattering (SAXS)/X-ray Diffraction (XRD)/XAFS combined technique frequently prioritizes capillary sample cell to fulfill the requirements of simultaneous measurements with multiple experimental techniques [16]. In such a combined measurement, the capillary sample cell is favorable for the XRD and SAXS measurements but not optimum for the XAFS measurement because of the variation in sample thickness or the X-ray path length passed through the sample. Unlike standard XAFS measurements at a uniform sample thickness, distortion and correction must be considered in the XAFS spectra collected by the capillary sample cell.

The transmission X-ray absorption spectrum (XAS) follows the Beer-Lambert Law [17], $I_t = I_0 exp(-\mu d)$., where I_0 is the incident X-ray intensity, I_t is the transmitted X-ray intensity, d is the length of the X-ray path in the sample or the physical thickness of the sample, and μ is the absorption coefficient of the material. In the range of X-ray energy nearing the absorption edge of the measured element in the sample, the X-ray absorption coefficient μ exhibits an oscillation structure known as XAFS signals. By extracting and analyzing the XAFS signals of a specific element, local coordination information, including the species of coordination atoms, coordination numbers, coordination distances, and the Debye-Waller factors, can be obtained. Experimentally, the transmission mode is commonly used to obtain the XAS curve [18-20]. Two gas ion chambers collect the incident X-ray intensity (I_0) and the transmission X-ray intensity (I_t), which are placed in front of and behind the sample, respectively [21, 22]. The measurement of transmission XAFS spectra requires uniform sample thickness. The literature has confirmed that the inhomogeneity of sample thickness distorts the

collected XAFS spectrum [23-25]. When a capillary sample cell is used to measure the transmission XAFS spectrum and two ion chambers without spatial resolution are used for the data acquisition of the XAFS spectra, the XAFS spectrum distortion caused by the cylindrical sample's different thicknesses is inevitable.

This study derives the distortion of the XAS curve caused by the capillary samples. On this basis, a possible method for correcting distorted XAFS spectra is proposed. The feasibility of collecting XAFS spectra using a capillary sample cell is discussed.

2. XAS Distortion

To consider the distortion of the XAS spectrum caused by the filling of the cylindrical sample in the capillary sample cell, a Cartesian coordinate system with the origin of the coordinates on the central axis of the capillary was established. The *x*-axis is along the axial direction of the capillary, the *y*-axis is in the vertically upward direction, and the *z*-axis is along the incident X-ray direction. In general, the incident X-ray beams are not perfectly parallel. The slight divergence (or focusing) degree of the incident X-ray beam results in slightly different path lengths of the X-rays through the sample, behaving as a similar thickness effect. This effect of beam divergence is not unique to capillary sample cells but is a commonly observed phenomenon in all XAFS measurements. To focus on the XAFS distortion caused by the capillary sample cell, we assumed that the incident X-rays were parallel beams. In addition, we assumed that the central axis of the incident X-ray beam was orthogonal to the central axis of the capillary. The transverse section of the capillary was in the *yOz* plane, as shown in Fig. 1.

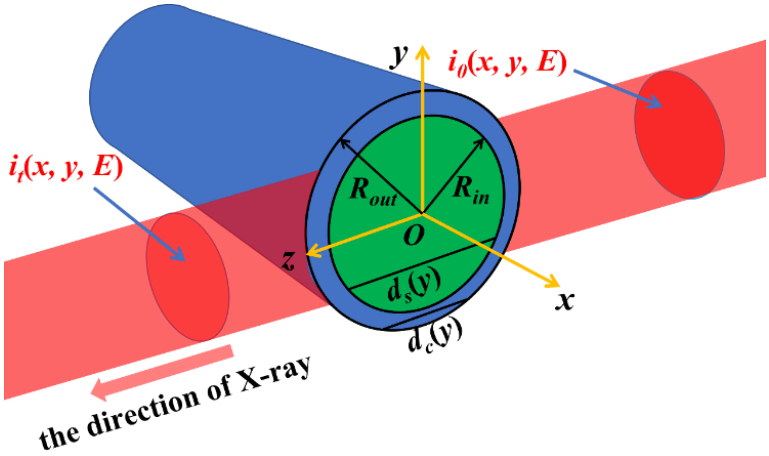

Figure 1. Geometric model of capillary sample cell used as XAS measurements. A Cartesian coordinate system was established, and parameters were defined for calculating and correcting the distortion of XAS spectra caused by the capillary.

For simplicity, the influence of the air path length change on X-ray absorption was not considered for the following reasons: First, the change in air path length caused by different thicknesses of the cylindrical samples is negligible. Second, the X-ray absorption caused by the air path of the capillary samples is basically the same as that of conventional flat-plate samples; therefore, no special consideration is required. Third, the X-ray absorption curve of the air path is monotonic, producing only monotonic variations in the background of the XAS curve, and no additional distortion is superimposed on the XAFS signals. Therefore, we did not consider X-ray absorption by the air path in the subsequent discussion of the distortion simulation and correction methods.

The inner and outer radii of the capillary are defined as R_{in} and R_{out}, respectively. Based on the geometric model of the capillary sample cell, as shown in Fig. 1, the X-ray path lengths in the sample and capillary wall are only dependent on the y-values and independent of the x-values and z-values. The X-ray absorption path lengths in the sample and capillary wall can be defined as $d_s(y)$ and $d_c(y)$, respectively, as shown in Eqs (1) and (2).

$$d_s(y)=\begin{cases}0, & R_{in}<y\\ 2\sqrt{R_{in}^2-y^2}, & -R_{in}<y<R_{in}\\ 0, & y<-R_{in}\end{cases}. \tag{1}$$

$$d_c(y)=\begin{cases}0, & R_{out}<y\\ 2\sqrt{R_{out}^2-y^2}-d_s(y), & -R_{out}<y<R_{out}\\ 0, & y<-R_{out}\end{cases}. \tag{2}$$

The absorption coefficients of the sample and capillary are defined as $\mu_s(E)$ and $\mu_c(E)$, respectively. In general, the incident X-ray intensity is not uniform in the transverse section of the incident X-ray beam and can be expressed as an intensity distribution $i_0(x, y, E)$ in the xOy plane. Similarly, the transmitted X-ray intensity is also not uniform in the transverse section of the transmitted X-ray beam. The transmission-beam X-ray intensity distribution can also be written as $i_t(x, y, E)$ in the xOy plane. However, X-ray intensities $i_0(x, y, E)$ and $i_t(x, y, E)$ at different locations on the transverse section of the incident and transmission X-ray beams cannot be obtained in real-time because the ion chambers used to measure the transmission XAFS spectrum do not have spatial resolution. X-ray intensity measured by the ion chamber is the total incident X-ray intensity $I_0(E)$ or the total transmission X-ray intensity $I_t(E)$. The former

is the integral of $i_0(x, y, E)$ over the entire xOy plane, and the latter is the integral of $i_t(x, y, E)$ over the entire xOy plane. In addition, the physical thickness of the sample $[d_s(y)]$ and the capillary wall $[d_c(y)]$ is not uniform only in the y direction; thus, the absorption thicknesses of the sample $[\mu_s(E)d_s(y)]$ and the capillary wall $[\mu_c(E)d_c(y)]$ only change along the vertical (y-axis) direction. Based on this discussion, we defined the incident X-ray intensity $I_0(E)$, transmission X-ray intensity $I_t(E)$, and projection $j_0(y, E)$ of the incident X-ray intensity along the y-axis as follows:

$$I_0(E) = \iint_{\infty} i_0(x, y, E)dxdy. \tag{3}$$

$$I_t(E) = \iint_{\infty} i_t(x, y, E)dxdy. \tag{4}$$

$$j_0(y, E) = \int_{-\infty}^{+\infty} i_0(x, y, E)dx. \tag{5}$$

The measured XAS curve, which comprises the distortion caused by the uneven thickness of the cylindrical sample, is described in Eq. (6).

$$\begin{aligned} \mu'(E)d_{eq} &= \ln\left[\frac{I_0(E)}{I_t(E)}\right] = \ln\left[\frac{I_0(E)}{\iint_{\infty} i_t(x, y, E)dxdy}\right] \\ &= -\ln\left[\int_{-\infty}^{+\infty} \frac{j_0(y, E)}{I_0(E)} e^{-\mu_s(E)d_s(y)-\mu_c(E)d_c(y)}dy\right]. \end{aligned} \tag{6}$$

In the equation above, d_{eq} is equivalent thickness of a cylindrical sample (i.e., the thickness when the cylindrical sample is equivalent to flat-plane sample), and $i_t(x, y, E) = i_0(x, y, E)\cdot\exp[-(\mu_s(E)d_s(y)+\mu_c(E)d_c(y))]$. The equivalent thickness of the cylindrical sample was determined using Eq. (6), which is related to the distribution of incident X-ray intensity but cannot be easily calculated from the capillary geometry. Eq. (6) shows the quantitative relationship between the measured X-ray absorption coefficient $\mu'(E)$, including distortion, and the real X-ray absorption coefficient $\mu_s(E)$ without distortion. According to Eq. (6), the distortion of the XAS curve is related to the capillary parameters $[d_s(y), d_c(y), \mu_c(E)]$ and the normalized incident X-ray intensity distribution $j_0(y, E)/I_0(E)$ in the vertical direction (y-axis).

3. Influence of XAS distortion

For further discussion, Eq. (6) can be taken as a function of distorted XAS spectra $\mu'd_{eq}$ versus real X-ray absorption coefficient $\mu_s d_{eq}$, namely, $\mu'd_{eq} = f(\mu_s d_{eq})$. For simplicity, energy E is not explicitly included in this function, because the expression

of $\mu' d_{eq}$ versus $\mu_s d_{eq}$ does not change with the incident X-ray energy. Therefore, in this study, the discussion of XAS distortion is available for each data point of an XAS curve. The three parameters μ_c, $d_s(y)$, and $d_c(y)$ in Eq. (6) are known in advance from the capillary parameters (μ_c, R_{in}, and R_{out}). $J_0(y) = j_0(y)/I_0$ is the normalized intensity distribution of the incident X-ray beam in the vertical direction. In general, $J_0(y)$ can be approximately simulated and replaced by a Hann function [26].

$$J_0(y) = \begin{cases} 0, & y-\varepsilon < -h \\ \frac{1}{2}\left[1-\cos\left(\frac{\pi(y-\varepsilon+h)}{h}\right)\right], & -h < y-\varepsilon < h \\ 0, & h < y-\varepsilon \end{cases}. \quad (7)$$

The Hann function is a symmetrical distribution function with its symmetrical axis at $y = \varepsilon$. In this study, $\varepsilon = 0$, which means the central axis of the incident X-ray beam, was assumed to pass through the central axis of the capillary. This assumption is not mandatory for deriving Eq. (6). If the central axis of the incident X-ray beam deviates distance ε from the central axis of the capillary, then it is sufficient that the normalized intensity distribution of the incident X-ray beam is expressed as $J_0(y-\varepsilon)$, no other changes are necessary. The full size of X-ray beam spot in the vertical direction is $2h$. The spatial distribution of X-ray beam spot intensity is also often simulated by a Gaussian function [27, 28]. The difference between the two functions is that the Gaussian function is defined in an infinite domain of $(-\infty, +\infty)$, and the Hann function is defined in a finite domain of $[\varepsilon - h, \varepsilon + h]$. Theoretically, X-ray leakage is inevitable in XAS measurements if the incident X-ray intensity distribution is in an infinite domain of definition. Therefore, the incident X-ray intensity distribution can be described as a function, such as the Hann function, with a finite domain of definition, which seems more appropriate for the XAS measurement of a cylindrical sample distributed in the inner diameter of a capillary tube than Gaussian function.

Under the different vertical sizes ($2h$) of the incident X-ray beam spot, the dependences of the distorted XAS spectrum $\mu' d_{eq}$ on the real X-ray absorption coefficient $\mu_s d_{eq}$ were calculated and shown in Fig. 2(a). These calculations were performed considering specific capillary parameters: $R_{in} = 0.5\ mm$, $R_{out} = 0.55\ mm$, $\varepsilon = 0\ mm$, and $\mu_c = 0.4\ mm^{-1}$. When the vertical size ($2h$) of the X-ray beam spot is infinitely close to zero, and $d_s = 2R_{in}$, $d_c = 2R_{out} - 2R_{in}$, $J_0(y) = 1$; then the function $\mu' d_{eq} = f(\mu_s d_{eq})$ converges to a straight line, which corresponds to the top line without any

distortion. The dependence of $\mu'd_{eq}$ on $\mu_s d_{eq}$ is approximately linear when the relative size h/R_{in} of the incident X-ray beam spot $2h$ to the inner diameter $2R_{in}$ of the capillary is smaller than 60%. This implies that the XAS data collected using the capillary sample cell can be used directly for XAFS analysis without further distortion correction.

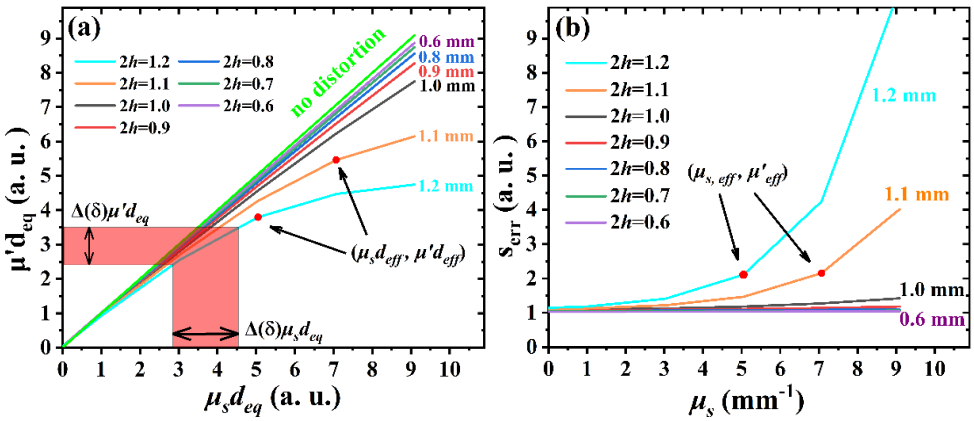

Figure 2. (a) Relationships between $\mu'd_{eq}$ and $\mu_s d_{eq}$, *i.e.*, the function of $\mu'd_{eq} = f(\mu_s d_{eq})$ with different vertical sizes of X-ray beam spot $2h$ under these capillary parameters $R_{in} = 0.5\ mm$, $R_{out} = 0.55\ mm$, $\varepsilon = 0\ mm$, and $\mu_c = 0.4\ mm^{-1}$. Generally, the μ_c value of the capillary is a monotonous and smooth function of energy E. When discussing the curve of $\mu' = f(\mu_s)$ defined by Eq. (6), $\mu_c(E)$ can be approximated to a constant. (b) Curves of defined error sensitivity function $s_{err}(\mu)$ with different vertical sizes of X-ray beam spot $2h$.

With an increase of $2h$, the distortion of the XAS became more pronounced. Figure 2(a) shows that the $\Delta\mu_s d_{eq}$ change is compressed to a reduced $\Delta\mu'd_{eq}$ change in the distorted XAS curve. Such an effect is called the "nonlinear compression effect", meaning the real XAS amplitude $\Delta\mu_s d_{eq}$ will be distorted to a reduced XAS amplitude $\Delta\mu'd_{eq}$ by a cylindrical sample. In other words, a smaller error $[\delta\mu'(\mathrm{E})d_{eq}]$ in the distorted XAS curve could be further amplified to a larger error $[\delta\mu_s(\mathrm{E})d_{\mathrm{eq}}]$ in the real XAS curve obtained by correcting the distorted XAS curve.

To further analyze the influence of the distortion caused by capillary sample cells with different inner diameters, the asymptotic behavior of Eq. (6), or the function $\mu'd_{eq} = f(\mu_s d_{eq})$, is discussed. First, the lengths of the X-ray path in the sample and capillary, and the intensity distribution of the incident X-rays, are symmetric functions for the central axis of the capillary (y=0) in the vertical direction. The integral range of Eq. (6) can be divided into two parts: from 0 to R_{in} and from R_{in} to infinity. When $0 < 2h \leq 2R_{in}$ (i.e., the vertical size of the X-ray beam spot is smaller than or equal to the inner diameter of the capillary), the distorted $\mu'd_{eq}$ increases towards infinity with an increase in real $\mu_s d_{eq}$, and there is no asymptotic behavior. When $2h > 2R_{in}$, the distorted XAS

$\mu'(E)d_{eq}$ increases towards a finite value, and the function $\mu' d_{eq} = f(\mu_s d_{eq})$ reveals an asymptotic behavior, as shown in Eq. (8).

$$\lim_{\mu_s d_{eq} \to \infty} f(\mu_s d_{eq}) = -\ln\left[2\int_{R_{in}}^{+\infty} \frac{j_0(y)}{I_0} e^{-\mu_c d_c(y)} dy\right]. \quad (8)$$

This asymptotic behavior demonstrates that as the real XAS signal ($\mu_s d_{eq}$) decreases, the distortion becomes smaller, or the consistency between $\mu' d_{eq}$ and $\mu_s d_{eq}$ improves. However, the X-ray absorption coefficient is an intrinsic property of the element and does not change with experimental conditions. This phenomenon implies that the smaller the equivalent thickness (d_{eq}) of the sample, the smaller the distortion. Specifically, when $\mu_s d_{eq}$ approaches 0, or the inner diameter of the capillary tube approaches 0, the distortion caused by a cylindrical sample on the measured XAS curve ($\mu' d_{eq}$) is negligible, confirmed by Fig. 2(a). By contrast, the intensity of the measured XAS signal ($\mu' d_{eq}$) would also approach 0 if the inner diameter of the capillary tube or $\mu_s d_{eq}$ approaches 0. This result implies that the larger the inner diameter of the capillary tube or the equivalent thickness d_{eq}, the better the XAS intensity. The conflicting requirements of the inner diameter of the capillary and the equivalent thickness of the sample indicate that the inner diameter of the capillary tube should be optimized to an ideal value. Using an edge jump of 1 ($\Delta\mu d$ =1) has been widely accepted as the ideal thickness of a flat-plane sample [29]. In a capillary sample system, introducing equivalent thickness d_{eq} enables the transmission X-ray intensity to be expressed identically to that of a flat-plane sample. The optimization of the sample thickness was exactly the same as that for the flat-plane sample. Therefore, the equivalent edge jump, $\Delta\mu_s d_{eq}$ =1, can also be used to determine the ideal inner diameter of the capillary tube. However, arbitrarily changing the inner diameter of the capillary tube is difficult. To a certain extent, edge jump $\Delta\mu_s d_{eq}$ can be adjusted by diluting the sample with low-density and relatively stable substances, such as boron nitride (BN). For a capillary tube with a fixed inner diameter, the available range of $\mu' d_{eq}$ used for extracting the absorption coefficient ($\mu_s d_{eq}$) should be limited.

To limit the available range that can be used to correct the distortion, we defined the knee point of curve $\mu' d_{eq} = f(\mu_s d_{eq})$ as the upper limit ($\mu_s d_{eff}$, $\mu' d_{eff}$) of the available effective data points. With the increase in the vertical size of X-ray beam spot $2h$, the upper limit ($\mu_s d_{eff}$, $\mu' d_{eff}$) of the available effective XAS value decreases. This attribute means correcting the distorted XAS curve becomes increasingly difficult as the X-ray

beam spot size increases. For a reasonable, quantitative evaluation, the error sensitivity s_{err} is defined as follows:

$$s_{err}\left(\mu_s d_{eq}\right)=\left(\frac{d(\mu' d_{eq})}{d(\mu_s d_{eq})}\right)^{-1}. \tag{9}$$

s_{err} represents error magnification. s_{err}= 0 indicates a complete insensitivity to errors. s_{err} < 1 indicates that the distortion correction reduces the error. s_{err} = 1 means that the error in the $\mu' d_{eq}$ curve is directly transferred to the $\mu_s d_{eq}$ curve without changing the magnitude of the error. s_{err} > 1 indicates that the distortion correction process amplifies the error. the $s_{\mathrm{err}}(\mu_s d_{eq})$ curves, corresponding to these curves of $\mu' d_{eq} = f(\mu_s d_{eq})$ with different $2h$ values, can be calculated and are illustrated in Fig. 2(b). The error sensitivity increases rapidly with the increase in $\mu_s d_{\mathrm{eq}}$ when $\mu' d_{eq} > \mu' d_{eff}$, especially in those cases of $2h > 2R_{in}$. Only when $2h < 2R_{in}$ can the error sensitivity be effectively suppressed at the low end of $\mu_s d_{\mathrm{eq}}$. When the distorted XAS curve ($\mu' d_{eq}$) is smaller than its upper limit ($\mu' d_{eff}$), the correction of the distorted XAS curve is reliable. Otherwise, the sample has to be diluted to fulfill the requirement of $\mu' d_{eq} < \mu' d_{eff}$.

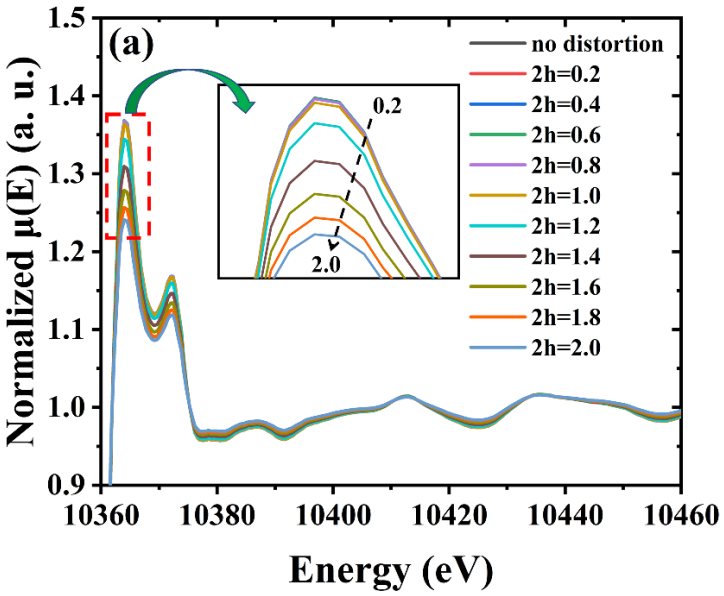

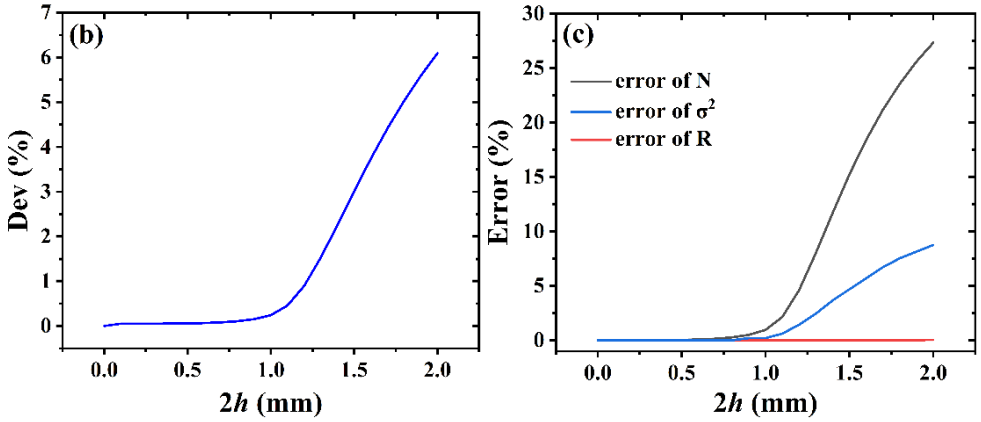

Figure 3. (a) Normalized distorted Ga K-edge XAS curve of gallium arsenide (GaAs) powder in a capillary: inner diameter, R_{in} = 0.5 *mm*, and outer diameter, R_{out} = 0.55 *mm*. Different vertical sizes ($2h$) of the incident X-ray beam spot were used to simulate the distorted XAS curves. (b) Change in deviation factors of the distorted XAS curve versus vertical sizes ($2h$) of the incident X-ray beam spot. (c) Changes in the relative errors of coordination number (N), coordination bond length (R), and Debye-Waller factor (σ^2) versus vertical size ($2h$) of the incident X-ray beam spot. Additional fitting results are in the supporting information.

For estimating the influence of the XAS distortion caused by the capillary sample cell on the XAS curve, the Ga K-edge XAS curve of the gallium arsenide (GaAs) powder without distortion was first collected with a flat-plane sample at beamline 4B9A of the Beijing Synchrotron Radiation Facility (BSRF). The storage ring run at 2.5 GeV with an electron-beam current of approximately 250 mA. The photon flux was approximately 1×10^{10} photons/s at the Cu-K-edge (8979 eV). A monochromatic incident X-ray beam was generated using a Si (111) double-crystal monochromator with an energy resolution ($\Delta E/E$) of approximately 3×10^{-4}. The GaAs sample was diluted with BN powder so that the edge jump was 1. The distorted XAS curves with different incident X-ray beam spot sizes ($2h$) can be simulated and calculated based on Eq. (6), as shown in Fig. 3(a), and used to assess the influence of distortion on the XAS curves. To observe the difference in those XAS curves, we present in Fig. 3(a) only the data points within a range from 0 to 100 eV relative to the absorption edge. The XAFS oscillations decrease more significantly with an increase in the beam spot size. However, only when $2h > 2R_{in}$ can the difference in the XAFS oscillations be easily observed. To quantify the magnitude of the distortion, we defined the deviation factor of the normalized distorted XAS curve $\mu'(E)d_{eq}$ from the normalized real XAS curve $\mu_{std}(E)d$ as

$$Dev = \left\{\frac{1}{n}\sum_{i=1}^{n}\left[\left|\frac{\mu'(E_i)d_{eq} - \mu_{std}(E_i)d}{\mu_{std}(E_i)d}\right|\right]\right\}\times 100\%. \qquad (10)$$

where n is the number of data points in $\mu'(E_i)d_{eq}$ or in the real XAS curve $\mu_{std}(E_i)d$. The change in deviation factor (Dev) with respect to the vertical size ($2h$) of the incident X-ray beam spot is shown in Fig. 3(b). The deviation factor increased slowly with an increase in the vertical size of the incident X-ray beam spot. When the vertical size of the incident X-ray beam spot increased to greater than the inner diameter of the capillary (i.e., $2h > 2R_{in}$), the deviation factor increased rapidly. Furthermore, structural parameters, including the coordination number (N), coordination bond length (R), and the Debye-Waller factor (σ^2), were determined by fitting the XAFS signals extracted from these distorted XAS curves. Relative errors N, R, and σ^2 depend on the vertical size ($2h$) of the incident X-ray beam spot, as shown in Fig. 3(c). Once again, when $2h > 2R_{in}$, the errors in these parameters caused by the cylindrical sample increase sharply. However, when $2h < 2R_{in}$, the errors in these structural parameters increased gradually with 2h. Based on a theoretically simulated XAS curve, the additional errors for structural parameters N, R, and σ^2 caused by the cylindrical sample in a capillary sample cell are estimated to be 0.07%, 0.00%, and 0.00%, respectively, if fixing h=0.6R_{in}, or 0.96%, 0.00%, and 0.20% if fixing h=R_{in}. This result demonstrates that the additional errors in the structural parameters were minute when considering only the shape effect of the cylindrical sample. However, the deviation of the X-ray path length from the ideal sample thickness in a cylindrical sample and the insufficient of high statistics for the weak edge intensity of the incident X-ray beam may be significant sources of error.

4. Correction of XAS Distortion

The main purpose of this study was to correct distorted XAS data caused by a cylindrical sample in a capillary sample cell. Thus, a correction method was proposed for XAS data distorted by a cylindrical sample in a capillary. The dependence of $\mu'd_{eq}$ on $\mu_s d_{eq}$ is shown in Fig. 2(a) and Eq. (6). When a capillary sample cell is used to collect the XAS curve; the collected XAS curve is distorted if the vertical size of the incident X-ray beam spot is sufficiently large (for example, $h > 0.6\ R_{in}$) compared to the inner diameter of the capillary. The corresponding measurement parameters, R_{in}, R_{out}, μ_c, and $2h$, were determined in advance. The relative intensity distribution of the incident X-ray beam spot $j_0(y, E)/I_0(E)$ can also be determined in advance or approximately simulated by the Hann function in Eq. (7) with the vertical size ($2h$) of the incident X-ray beam spot. Therefore, the relationship between $\mu'd_{eq}$ and $\mu_s d_{eq}$ can be determined.

That is, each data point in the distorted XAS curve ($\mu' d_{eq}$) always has a corresponding data point in the real XAS curve ($\mu_s d_{eq}$). Such a corresponding relation between $\mu' d_{eq}$ and $\mu_s d_{eq}$, as shown in Fig. 2(a), can be used to correct the distorted XAS curve.

In beamline 4B9A of the BSRF, the distorted XAS data were first collected using a cylindrical powder sample packed in a capillary. The synchrotron radiation conditions for the experimental measurements were identical to those described in Section 3 for the XAS measurement of a flat sample. High-purity amorphous SiO_2 (fused silica) capillary tubes with an inner diameter ($2R_{in}$) of 1.0 mm and an outer diameter ($2R_{out}$) of 1.1 mm were selected for the measurements. Its X-ray absorption coefficient $\mu_c(E)$ is known [30]. The capillary tube filled with BN-diluted GaAs powder was placed horizontally and perpendicular to the incident X-ray beam. The central axis of the capillary was adjusted to coincide with the center of the incident X-ray beam. The K-edge XAS curves of Ga were collected at vertical X-ray beam spots 0.8, 1.0, 1.5, 2.5, and 3.7 mm and labeled D0.8, D1.0, D1.5, D2.5, and D3.7, respectively. For reference, the Ga K-edge XAS data of a standard GaAs plates were collected under the same experimental conditions and labeled Ga-std.

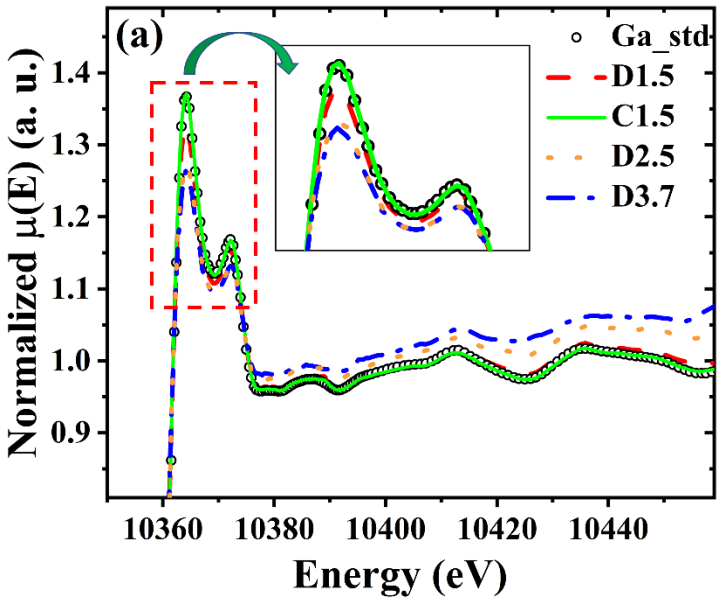

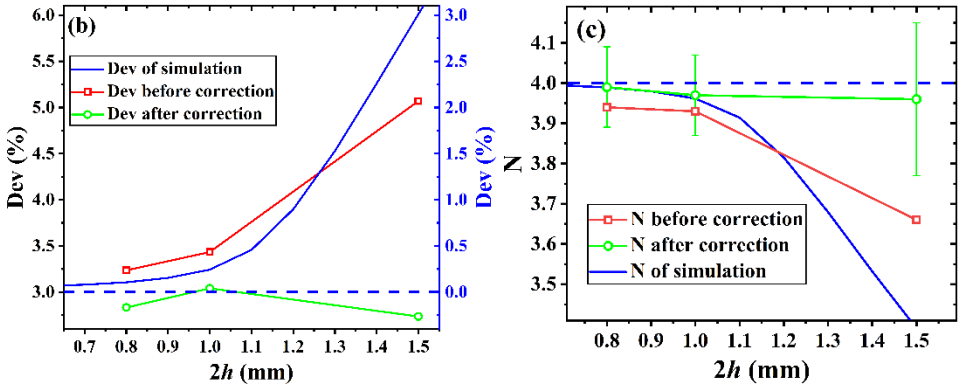

Figure 4. (a) Normalized XAS curves for distorted samples D1.5 (red dash line), D2.5 (orange dot line), D3.7 (blue dash-dot line), the corrected sample C1.5 (solid green line), and the reference sample Ga-std (black circles). (b) Deviation factors of distorted XAS curves D0.8, D1.0, and D1.5 (hollow red squares, left axis); corrected XAS curves C0.8, C1.0, and C1.5 (hollow green circles, left axis); and simulated XAS distortion curves (solid blue line, right axis). (c) Coordination numbers of Ga-As obtained by fitting the normalized XAFS spectra of distorted samples D0.8, D1.0, and D1.5 (red hollow squares); corrected samples C0.8, C1.0, and C1.5 (green hollow circles); and the simulated XAS distortion curves (blue solid line).

When the vertical cross-section size of the incident X-ray beam was greater than the inner diameter of the capillary tube ($h > R_{in}$), some data points in D2.5 and D3.7 did not fulfill the requirement of $\mu' d_{eq} < \mu' d_{eff}$ constraint; thus, the experimental error of these data points will be greatly amplified after distortion correction, resulting in the unreliable correction values for D2.5 and D3.7. This result confirms that the correction of the distorted XAS data fails if the vertical size of the incident X-ray beam spot is too large. The distorted XAS curves D1.5 (red dashed line), D2.5 (orange dotted line), and D3.7 (blue dashed-dotted line); the corrected XAS curve C1.5 (solid green line); and the reference XAS data Ga-std (black circles) without distortion were compared, as shown in Fig. 4(a). To indicate the differences among the three XAS curves, only the data within the range of 0 to 100 eV relative to the Ga absorption K-edge are shown. The difference between the distorted XAS curve and the corrected XAS curve was observed. Although the vertical size ($2h$=1.5 mm) of the incident X-ray beam spot was still very large and the distortion was severe, a high degree of agreement was observed between the corrected XAS curve and the reference XAS curve. This result demonstrates that the correction method partially corrected the distortion caused by the cylindrical sample in the capillary sample cell.

To further verify the effectiveness of this distortion correction, we compared the deviation factors of the distorted XAS curves (D0.8, D1.0, D1.5) with those of the corrected XAS curves (C0.8, C1.0, C1.5); these deviation factors before and after correction are shown in Fig. 4(b). The deviation factor increased with increasing X-ray

beam spot size, particularly for distorted XAS curves with $2h > 2R_{in}$. After the distortion correction, the deviation of the corrected XAS curves from the real or standard XAS curves improved significantly. For comparison, the deviation factors of the simulated XAS curves are shown in Fig. 4(b). The deviation factors of the distorted XAS curves acquired experimentally before correction were significantly greater than those of the simulated XAS curves. The main reason for this difference is the influence of other experimental factors, excluding the capillary sample shape. These additional factors resulted in the distorted XAS curves having higher statistical noise or additional distortion in the experiment; by contrast, the simulated XAS curves had no statistical noise and were not affected by other experimental factors. For a further comparison, the XAFS oscillations were extracted from the distorted and corrected XAS curves. The extracted XAFS spectra were routinely analyzed to determine near-neighbor structural parameters. The coordination numbers obtained from these XAFS oscillations are compared in Fig. 4(c). GaAs has a zincblende-type crystal structure, in which each Ga atom is surrounded by four As atoms; inversely, each As atom is surrounded by four Ga atoms [31]. The coordination numbers extracted from the distorted XAS curves (D0.8, D1.0, D1.5) are lower than the real coordination number (N=4). The greater the incident X-ray beam spot, the greater the deviation of the coordination number. However, the coordination numbers extracted from the corrected XAS curves (C0.8, C1.0, C1.5) were closer to the actual value of 4. The deviation factors and coordination numbers calculated from the simulated XAS curves are compared in Fig. 3(b)-3(c), respectively.

Inhomogeneous X-ray paths cause a thickness effect that attenuates the amplitude of XAFS oscillations [23-25]. However, amplitude attenuation mainly leads to an underestimation of the coordination number. As shown in Fig. 4(c), the underestimation of the coordination number slowly becomes serious as the incident X-ray beam spot size increases but rapidly deteriorates when the incident X-ray beam spot size is greater than the inner diameter of the capillary tube. We compared these underestimated values of the coordination number with the theoretically predicted errors shown in Fig. 3(c). The underestimated values of the fitted coordination number of the experimentally distorted XAFS spectra appeared to be within the error of the correction value when $2h$ was greater than $2R_{in}$ but beyond the error when $2h$ was less than or equal to $2R_{in}$. Evidently, the fitting parameters for the experimental XAFS spectra without distortion correction are limited not only by the influence of inhomogeneous thickness but also

by other experimental factors, for example, the fluctuation of X-ray intensity and divergence. In general, the experimental errors are always larger than the theoretically predicted values. The estimated error bars for the distortion-corrected coordination numbers are shown in Fig. 4(c). Based on the aforementioned discussion, we posit that correction of the distorted XAS curve is reasonable only when the size of the incident X-ray beam spot is smaller than the inner diameter of the capillary tube. In other words, XAS measurements with $2h>2R_{in}$ should be avoided. This study demonstrates that this correction method for distorted XAS curves is feasible and acceptable only when the size of the incident X-ray beam spot is smaller than the inner diameter of the capillary tube. Additional fitting details are presented in Fig. S1 and Tab. S. In this study, only the distortion of XAS data caused by a cylindrical sample in a capillary sample cell was considered. The influence of other factors, for example, instrument error and signal-to-noise ratio [32-33], is a topic for further research.

Conclusion

The distortion of the XAS should be considered when a capillary sample cell is used to collect XAS. In this study, the dependence $\mu'(E)d_{eq}=f[\mu_s(E)d_{eq}]$ of the distorted XAS curves $\mu'(E)d_{eq}$ on the real XAS curves $\mu_s(E)d_{eq}$ was derived. Based on the known conditions, including the inner diameter R_{in}, the outer diameter R_{out}, the X-ray absorption coefficient of capillary $\mu_c(E)$, and the intensity distribution on the cross-section of the incident X-ray beam, the correction curve of $\mu'd_{eq}=f(\mu_s d_{eq})$ can be calculated. A corrected method for the distorted XAS curve was proposed and was identified as feasible. This suggests that the distorted XAS data can be used for distortion correction only when the vertical size ($2h$) of the incident X-ray beam spot is smaller than the capillary tube's inner diameter ($2R_{in}$). When $h/R_{in} < 0.6$, distortion can be ignored. In addition, this correction method can be applied to XAS measurements of other sample systems with inhomogeneous thicknesses if the thickness change in the sample can be mathematically expressed.

Acknowledgements

This study was supported by the National Key R&D Program of China (grant numbers 2022YFA1603802 and 2017YFA0403000). This study was performed on beamlines 1W2B and 4B9A at the Beijing Synchrotron Radiation Facility.

Supporting information are available

Based on Eq. (6), Python scripts were supplied, as shown in Scripts 1 & 2, which can simulate and correct distorted XAFS spectra.

ASSOCIATED CONTENT

Author information

Corresponding Author

*E-mail: wuzh@ihep.ac.cn; Phone: 86-10-88235982.

*E-mail: mog@ihep.ac.cn; Phone: 86-10-88235993.

ORCID

Zhonghua Wu: 0000-0002-8036-022X

Guang Mo: 0000-0002-1278-5904

Notes

The authors declare no competing financial interest.

References

1. Z. Sun, Q. Liu, T. Yao et al., X-ray absorption fine structure spectroscopy in nanomaterials. China. Mater. **58**, 313-341 (2015). doi: 10.1007/s40843-015-0043-4
2. S. Q. Wei, Z. H. Sun, Z. Y. Pan et al. XAFS applications in semiconductors. Nucl. Sci. Tech. **17**, 370-388 (2022). doi: 10.1016/S1001-8042(07)60006-2
3. H. Zhu, Y. Huang, H. Zhu et al. In Situ Probing Multiple-Scale Structures of Energy Materials for Li-Ion Batteries. Small. Methods. 1900223 (2019). doi: 10.1002/smtd.201900223
4. W. Li, M. Li, Y. Hu et al. Synchrotron-Based X-ray Absorption Fine Structures, X-ray Diffraction, and X-ray Microscopy Techniques Applied in the Study of Lithium Secondary Batteries. Small. Methods. 2, 1700341 (2018). doi: 10.1002/smtd.201700341
5. Z. L. Gong, Y. Yang, The application of synchrotron X-ray techniques to the study of rechargeable batteries. J. Energy. Chem. **27**, 1566-1583 (2018). doi: 10.1016/j.jechem.2018.03.020
6. Q. Yang, Q. Li, Z. Liu et al., Dendrites in Zn-Based Batteries. Adv. Mater. **32**, 2001854 (2020). doi: 10.1002/adma.202001854
7. Z. B. Wu, W. K. Pang, L. B. Chen et al., In Situ Synchrotron X-Ray Absorption Spectroscopy Studies of Anode Materials for Rechargeable Batteries. Batteries. Supercaps. **4**, 1547-1566 (2021). doi: 10.1002/batt.202100006
8. X. P. Sun, F. F. Sun, S. Q. Gu et al., Local structural evolutions of $CuO/ZnO/Al_2O_3$ catalyst for methanol synthesis under operando conditions studied by in-situ quick X-ray absorption spectroscopy. Nucl. Sci. Tech. **28**, 21 (2017). doi: 10.1007/s41365-016-0170-y
9. Q. Chang, K. Li, C. H. Zhang et al., XAFS Studies of Fe–SiO_2 Fischer-Tropsch Catalyst During Activation in CO, H_2, and Synthesis Gas. ChemCatChem. **11**, 2206–2216 (2019). doi: 10.1002/cctc.201801807.
10. D. B. Liu, Q. He, S. Q. Ding et al., Structural Regulation and Support Coupling Effect of Single-Atom Catalysts for Heterogeneous Catalysis. Adv. Energy. Mater. **10**, 2001482 (2020). doi: 10.1002/aenm.202001482.
11. X. Y. Wang, X. B. Peng, H. Y. Ran et al., Influence of Ru Substitution on the Properties of $LaCoO_3$ Catalysts for Ammonia Synthesis: XAFS and XPS Studies. Ind. Eng. Chem. Res. **57**, 17375–17383 (2018). doi: 10.1021/acs.iecr.8b04915
12. Z. H. Wu, Y. P. Liu, X. Q. Xing et al., A Novel SAXS/XRD/XAFS Combined Technique for in-Situ Time-Resolved Simultaneous Measurements. Nano Res. 1-9 (2022). doi: 10.1007/s12274-022-4742-3
13. X. Li, H. Y. Wang, H. Yang et al., In situ/operando characterization techniques to probe the electrochemical reactions for energy conversion. Small. Methods. **2**, 1700395 (2018). doi: 10.1002/smtd.201700395
14. H. E. Piskorska, D. A. Kowalska, P. Kraszkiewicz et al., In Situ XAFS Study of Highly Reducible Mixed Oxide Catalysts $Ce_{0.9}Pd_{0.1}O_{2-\delta}$ and $Ce_{0.7}Yb_{0.2}Pd_{0.1}O_{2-\delta}$. J. Alloys Compd. **831**, 154703 (2020). doi: 10.1016/j.jallcom.2020.154703
15. A. Bansode, G. Guilera, V. Cuartero et al., Performance and Characteristics of a High Pressure, High Temperature Capillary Cell with Facile Construction for Operando x-Ray Absorption Spectroscopy. Rev. Sci. Instrum. **85**, 084105 (2014). doi: 10.1063/1.4893351
16. H. Wang, G. Mo, J, J, Zhong et al., A Capillary Sample Cell Used for In-Situ SAXS, XRD, and XAFS Measurements during Hydrothermal Synthesis. Nucl. Instrum. Methods Phys. Res. Sect.

Accel. Spectrometers Detect. Assoc. Equip. **1031**, 166605 (2022). doi: 10.1016/j.nima.2022.166605
17. T. G. Mayerhöfer, S. Pahlow, J. Popp., The Bouguer-Beer-Lambert Law: Shining Light on the Obscure. ChemPhysChem. **21**, 2029–2046 (2020). doi: 10.1002/cphc.202000464
18. H. S. Yu, X. J. Wei, J. Li et al., The XAFS beamline of SSRF. Nucl. Sci. Tech. **26**, 050102 (2015). doi: 10.13538/j.1001-8042/nst.26.050102
19. R. Y. Lu, Q. Gao, S. Q. Gu et al., Data-collection system for high-throughput X-ray absorption fine structure measurements. Nucl. Sci. Tech. **27**, 82 (2016). doi: 10.1007/s41365-016-0084-8
20. P. Q. Duan, H. L. Bao, J. Li, et al., In-situ high energy resolution X-ray absorption spectroscopy for UO2 oxidation at SSRF. Nucl. Sci. Tech. **28**, 2 (2017). doi: 10.1007/s41365-016-0155-x
21. G. F. Knoll, Radiation Detection and Measurement. John Wiley & Sons. (2010). https://www.wiley.com/en-us/Radiation+Detection+and+Measurement%2C+4th+Edition-p-9780470131480
22. Y. P. Liu, L. Yao, B. J. Wang, et al., Silicon PIN photodiode applied to acquire high-frequency sampling XAFS spectra. Nucl. Sci. Tech. **33**, 91 (2022). doi: 10.1007/s41365-022-01066-2
23. E. A. Stern, K. Kim. Thickness Effect on the Extended-X-Ray-Absorption-Fine-Structure Amplitude. Phys Rev B. **23**, 3781–3787 (1981). doi: 10.1103/PhysRevB.23.3781
24. A. Manceau, M. A. Marcus, N. Tamura, Quantitative Speciation of Heavy Metals in Soils and Sediments by Synchrotron X-Ray Techniques. Rev. Mineral. Geochem. **49**, 341–428 (2002). doi: 10.2138/gsrmg.49.1.341
25. L. G. Parratt, C. F. Hempstead, E. L. Jossem, “Thickness Effect” in Absorption Spectra near Absorption Edges. Phys Rev. **105**, 1228–1232(1957). doi: 10.1103/PhysRev.105.1228
26. P. Kahlig, Some Aspects of Julius Von Hann’s Contribution to Modern Climatology. Interactions Between Global Climate Subsystems: The Legacy of Hann. **75**, 1–7 (1993). doi: 10.1029/GM075p0001.
27. J. Chalupský, L. Juha, J. Kuba et al., Characteristics of Focused Soft X-Ray Free-Electron Laser Beam Determined by Ablation of Organic Molecular Solids. Opt. Express. **15**, 6036–6043 (2007). doi: 10.1364/OE.15.006036
28. J. Chalupský, J. Krzywinski, L. Juha et al., Spot Size Characterization of Focused Non-Gaussian X-Ray Laser Beams. Opt. Express. **18**, 27836–27845 (2010). doi: 10.1364/OE.18.027836
29. M. Newville et al., Fundamentals of XAFS. Rev. Mineral. Geochem. **78**, 33-74 (2014). doi: 10.2138/rmg.2014.78.2
30. B. L. Henke, E. M. Gullikson, J. C. Davis, X-Ray Interactions: Photoabsorption, Scattering, Transmission, and Reflection at E = 50-30,000 EV, Z = 1-92. At. Data Nucl. Data Tables. **54**, 181–342 (1993). doi: 10.1006/adnd.1993.1013
31. McCluskey, D. Matthew, E. E. Haller, Dopants and Defects in Semiconductors. CRC press, (2018). https://www.routledge.com/Dopants-and-Defects-in-Semiconductors/McCluskey-McCluskey-Haller-Haller/p/book/9780367781439
32. J. Goulon, G. Ginet, C. C. Robert et al., On Experimental Attenuation Factors of the Amplitude of the EXAFS Oscillations in Absorption, Reflectivity and Luminescence Measurements. J. Phys. **43**, 539–548 (1982). doi: 10.1051/jphys:01982004303053900
33. N. V. Bausk, S. B. Erenburg, L. N. Mazalov, Correction of XAFS Amplitude Distortions Caused by the Thickness Effect. J. Synchrotron Radiat. **6**, 268–270. doi: 10.1107/S0909049599001399

(1999). doi: 10.1107/S0909049599001399